JOURNAL OF MATERIALS SCIENCE **34** (1999) 481–495

Interfacial phenomena in glass fibre reinforced polyester resin with low profile additives

Part I *Micromechanical evaluation by pull out testing*

C. DELFOLIE, C. DEPECKER, J. M. LEFEBVRE
Laboratoire Structure et Propriétés de l'Etat Solide, URA CNRS234, UST Lille, 59655 Villeneuve d'Ascq cedex, France
E-mail: Jean-Marc.Lefebvre@univ-lillel.fr

The interfacial response of a glass fibre/unsaturated polyester resin matrix composite has been evaluated by means of single fiber pull-out tests. The nature of fibre sizing, more specifically sizing solubility, affects the debonding behavior. A confrontation of experimental data to current micromechanical models, assuming either mechanical or energetic criteria, proves quite efficient in relating stability of the debonding process to sizing characteristics.

Nomenclature

a	crack length
α	an elastic constant
	$\alpha_1 = \sqrt{\dfrac{2\mu}{b_i r_f E_f}}$
	$\alpha_2 = \sqrt{\dfrac{2\mu_m}{r_f^2 E_f \ln(R/2r_f)}}$
	$\alpha_3 = \sqrt{\dfrac{4\pi\mu_m}{E_f \ln(R/r_f)}}$
β	a constant of Yue *et al.*'s model
b_i	effective thickness of fibre-matrix interface
C	compliance
E_f	modulus of elasticity of the fibre
E_m	modulus of elasticity of the matrix
F_d	debond load
G_i	interfacial toughness
H	constant of the shear-lag theory
L	embedded length
L_d	debonded length
m	a constant of Hsueh's model
μ	coefficient of friction
μ_i	interface shear modulus
μ_m	matrix shear modulus
ν_f	Poisson's ratio of the fibre
ν_m	Poisson's ratio of the matrix
P_0	axial load applied to the fibre
ψ	an elastic constant of Yue *et al.*'s model
q_0	clamping stress on the fibre
r_f	fibre radius
R_m	matrix outer radius
σ_d	complete debond stress
σ_d^p	partial debond stress
σ_f	axial stress to pull out a fibre
τ	interfacial shear stress
τ_a	average interfacial shear strength
τ_d	interfacial shear strength
τ_f	interfacial shear stress due to friction
τ_{max}	maximum of the interfacial shear stress
z_{max}	critical bonded length

1. Introduction

The mechanical properties of fibre reinforced composites strongly depend on the specific properties of the matrix and reinforcing fibers. However, a simple model based on matrix and fibre mechanical data cannot account for the composite behavior. Indeed, a third component appears when matrix and fibre are brought into contact, the interface.

Its role is of prime importance because it ensures stress transfer between matrix and fibres. Moreover, the interface is the locus of singular behaviors. First, from a mechanical point of view, introducing fibres in a polymer matrix leads to stress concentrations produced by external loads applied to the material, shrinkage stresses created during curing and thermal residual stresses. Second, specific intermolecular fibre-matrix interactions may be responsible for matrix microstructural changes in the vicinity of the reinforcing element.

This last point is relevant to the concept of interphase. Whereas interface reveals the discontinuity between matrix and fibre (thickness equal to zero), the interphase is the three-dimensional zone near the fibre in which properties are different from bulk matrix ones. Therefore, proper control of the physical properties of composite materials requires to understand physicochemical phenomena occurring during interface formation, to characterize its final microstructure and to determine how it may affect the mechanical properties.

The nature of the interface has a large influence on both the mode of failure and toughness of composite materials. A strong interface with a high value of the interfacial shear strength τ_d would promote crack propagation across the fibres, whilst a poor fibre-matrix

bonding would promote failure by fibre debonding and pull out [1, 2]. The improvement of composites toughness has been attributed to the latter mechanisms [3, 4]. In contrast, a good adhesion reduces toughness while increasing compressive strength, flexural strength and off-axis strength [5, 6]. Along these lines, the objectives of the present work are to characterize glass fibre reinforced unsaturated polyester composites in terms of interfacial parameters which include the shear strength τ_d, the interfacial toughness G_i, the matrix shrinkage pressure q_0 on the fibre and the interfacial friction coefficient μ.

Although interfacial strength can be evaluated from unidirectional composite behavior, the results are strongly dependent on such factors as the specimen geometry and the fibre volume fraction. Moreover, a single and simple mode of testing cannot be performed because of the complexity of stress distribution in non isotropic materials.

The use of single filament specimen provides a more convenient model system, the major advantage of such samples being to allow direct measurement of interfacial parameters. Different levels of adhesion can be discriminated by single filament tests [7], which in some instances enable to correlate between micromechanical and macromechanical data [8, 9]. Moreover, fundamental informations about debonding process can be obtained and help to understand macrocomposite behavior [10].

Notwithstanding, the results are strongly dependent on experimental procedure [7] and consequently the computed interfacial parameters values must not be considered as absolute ones.

The main micromechanical techniques are the fragmentation test, the microindentation test, the microdebond test and the pull-out test. In the fragmentation test [5, 7, 11–16], a fibre is carefully aligned down the center of a dog-bone shape sample. The latter is loaded in tension and its deformation leads to multiple fibre failure until saturation of fibre failure process is reached. The fragment lengths are measured at the end of the test.

In the microindentation test method [5, 7, 17–18], an indentor is used to cause fibre debonding in thin sections of unidirectional composites.

In the microdebond test [5, 7, 14, 15], liquid matrix drops are deposited on the fibre. After matrix curing, the drop is placed between two knife edges and debonding is obtained by an applied tensile load on the fibre.

The pull out test has been retained in the present work. A single fibre is embedded in a block of resin. The fibre is pulled from the cured resin by tensile loading on the fibre.

The latter method is one of the most direct manner for measuring interfacial parameters. Nevertheless, the analysis and interpretation of the experimental data turn out to be a complicated task considering the numerous theoretical models that have been developed for modelling the pull-out test. A critical review focusing at the theoretical assumptions will be made. Two very attractive approaches will be considered and confronted with experimental results.

2. Interface micromechanics

The fibre pull out from a matrix block is the consequence of two phenomena: debonding and post-debonding friction of the fibre against the debonded surfaces. According to some authors, debonding can be considered either complete or partial. In the case of a partially debonded fibre, friction parameters must be taken into account in the analysis.

Theoretical analysis of the pull-out test can be classified into two kinds of approach. In a mechanical approach based on a maximum shear stress criterion, the interface fails when the interfacial shear stress exceeds the debond shear strength τ_d. In an energy-based approach, the interface is characterized by its work of fracture G_i. Both will be discussed separately in the two following subsections and the friction behavior will be the subject of a third one.

2.1. Mechanical approach

The interface fails when the interfacial shear stress exceeds the critical value τ_d. Consequently, the shear stress distribution along the interface needs to be evaluated.

A uniform shear stress along the interface [19] is often assumed as a first approximation, but this is only achieved when the matrix is totally plastic. The interfacial shear strength is given by:

$$\tau_d = \frac{F_d}{2\pi r_f L} \tag{1}$$

Greszczuk [20, 21] has derived the distribution of the shear stress along the fibre length in the case of an elastic matrix. The fibre is embedded in a semi-infinite matrix to a length L and an axial load P_0 is applied to the fibre (Fig. 1).

The fibre-matrix bonding is assumed to be perfect (no sliding along the interface). The shear stress τ is expressed as a function of interface thickness b_i and interface shear modulus μ_i. Greszczuk has assumed that the embedded fibre end carries no load ($P(x = L) = 0$). The shear stress along the embedded fiber is given by:

$$\tau(x) = \frac{P_0\alpha}{2\pi r_f}[\sinh(\alpha x) - \coth(\alpha L)\cosh(\alpha x)] \tag{2}$$

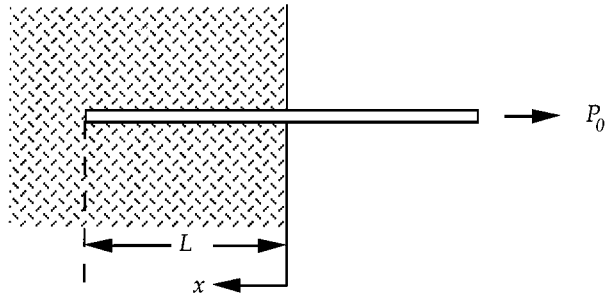

Figure 1 Semi-infinite pull-out configuration.

with

$$\alpha = \alpha_1 = \sqrt{\frac{2\mu_i}{b_i r_f E_f}} \tag{3}$$

In this model, the maximum of the shear stress τ_{max} is reached at the point where the fibre enters the matrix. The interface fails when $\tau_{max} \geq \tau_d$. The average shear strength can be defined as:

$$\tau_a = \frac{F_d}{2\pi r_f L} = \tau_d \frac{\tanh(\alpha L)}{\alpha L} \tag{4}$$

Lawrence [22] reconsidered the shear stress distribution along the embedded fibre. This time, the shear stress τ is given by $\tau \propto H(u - v)$, u is the virtual displacement in the direction of the fibre at a point in the fibre at a distance $(L - x)$ from the embedded end if the matrix had the same elastic properties as the fiber, v is the virtual displacement of the matrix at the same point if the fibre was replaced by the matrix and H is a constant from Cox shear-lag theory [23]. The calculation leads to an expression of the shear stress distribution similar to that given by Greszczuk (Equation 2), only the constant α is changed and is given by:

$$\alpha = \alpha_2 = \sqrt{\frac{2\mu_m}{r_f^2 E_f \ln(R/2r_f)}} \tag{5}$$

with R, the radius of the matrix involved in shear strain.

Takaku and Arridge [24] have developped a similar model assuming that the shear stress τ is equal to Hu.

Then the constant α becomes:

$$\alpha = \alpha_3 = \sqrt{\frac{4\pi\mu_m}{E_f \ln(R/r_f)}} \tag{6}$$

In the three latter models, the fibre is considered to be embedded in a semi-infinite matrix. When the fibre is embedded in a coaxial matrix cylinder of outer radius R_m (Fig. 2) the mechanical equilibrium between the external load and the internal stress distribution in any section of the composite must be considered.

Yue and Cheung [25, 26] have derived the expression of interfacial shear stress in this case:

$$\tau(z) = \frac{P_0}{2\pi r_f}\left\{\beta(1-\psi)\exp(-\beta z) + \left[\psi + (1-\psi)\exp(-\beta L)\frac{\beta\cosh(\beta z)}{\sinh(\beta L)}\right]\right\} \tag{7}$$

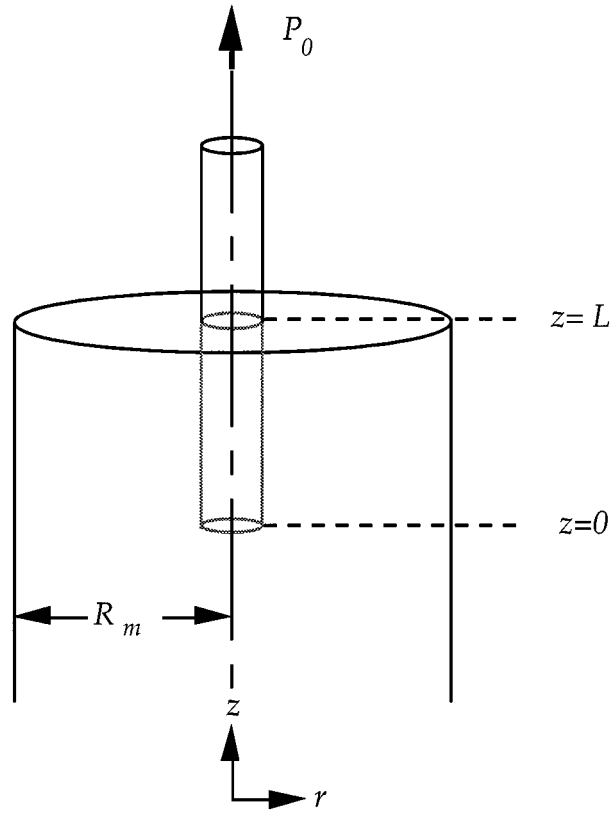

Figure 2 Finite pull-out configuration.

β and ψ are two constants which depend on the Young's moduli of matrix and fiber and the composite component sizes.

According to this model, the location of interfacial crack initiation depends on both the relative modulus of the matrix and fibre (E_f/E_m) and the relative size of the fibre and the matrix (R_m/r_f). In a composite system with either a large (E_f/E_m) ratio or a small (R_m/r_f) ratio, the interfacial shear stress is maximum at the end of the embedded fibre. Crack initiation at this particular location has been observed in glass/silicon [27] and in nylon/ethylene-propylene [28] systems. In composites with a small (E_f/E_m) ratio and a large (R_m/r_f) ratio, crack initiation occurs at the point where the fibre enters the matrix and the debonding strength is given by:

$$\tau_d = \frac{F_d}{2\pi r_f}\{\beta(1-\psi)\exp(-\beta L) + [\psi + (1-\psi)\exp(-\beta L)]\beta\coth(\beta L)\} \tag{8}$$

The common assumption to all models discussed above is that the embedded fibre end carries no load. Hsueh [29] has taken into consideration the continuity of deformation at the embedded fibre end, so that the load at $z = 0$ is not equal to zero. The interfacial shear strength is then:

$$\tau = \frac{P_0}{\pi r_f^2}\left\{-\frac{r_f}{2}\left(\frac{R_m^2}{r_f^2} - 1\right)\frac{E_m}{E_f}\sqrt{(1+\nu_m)\left[1 + \left(\frac{R_m^2}{r_f^2} - 1\right)\frac{E_m}{E_f}\right]\left[R_m^2 \ln\left(\frac{R_m}{r_f}\right) - \frac{R_m^2 - r_f^2}{2}\right]\tanh(mL)}\right\} \tag{9}$$

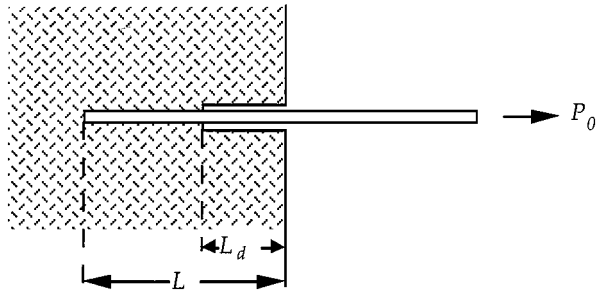

Figure 3 Partially debonded fibre pull-out configuration.

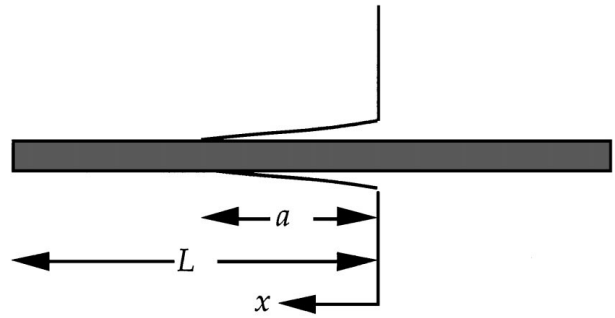

Figure 4 Schematic view of crack propagation along the interface.

with m being a constant which depends on the moduli of composite components, the Poisson's ratio of the matrix and the composite component sizes.

The load at the end of the embedded fibre is constant whatever the embedded length. Désarmot and Favre [30] have pointed out that this assumption is not satisfactory when $L \to \infty$.

All the above-mentioned analyses assume a complete debonding along the interface. Lawrence [22] introduced the concept of a partial fibre-matrix debonding. When the maximum of interfacial shear stress is reached, debonding is initiated at the point where the fibre enters the matrix (a small E_f/E_m ratio is assumed), and either the catastrophic debonding occurs at a constant load or a further increase in load is necessary for debonding to continue. The factors which control the nature of debonding are determined when a partially debonded fibre configuration (Fig. 3) is considered.

In this case, the contribution to the load transfer process of frictional resistance forces acting over the debond zone L_d must be taken into account in the analysis. Lawrence assumed an interfacial shear stress due to friction τ_f constant over the whole debonded area, and he showed that the stage at which debonding becomes catastropic is dependent on the ratio τ_d/τ_f and the debonded length L_d. Yue and Cheung [25] have theoretically deduced a critical value z_{max} of $(L - L_d)$: as soon as $z_{max} = (L - L_d)$, catastrophic debonding occurs. Hsueh [31] also introduced partial debonding in his analysis and considered the Poisson's contraction of the loaded fibre. In this case, the interfacial shear stress due to friction is no more constant over the debond region. The shear stress distribution has been recalculated on the basis of his latter model [29].

Some more complicated theoretical models have been developed [32–34], Nevertheless they do not provide a major improvement in experimental data analysis. On the contrary, finite element computation of the shear stress distribution has allowed the validation of a simple model as Greszczuk's one [30].

2.2. Energetic approach

The interface is characterised by its fracture toughness G_i. Debonding is due to a crack propagation along the interface (Fig. 4).

In the pull-out configuration, the Griffith fracture criterion is given by:

$$\frac{1}{2}\frac{\partial C}{\partial a}F_d^2 da = 2\pi r_f G_i \qquad (10)$$

Exact solution for the compliance C as a function of crack length is not available, but using an approximate expression for compliance, the debond stress in the elastic case can be given by [2, 3, 35]:

$$\sigma_d = \frac{F_d}{\pi r_f^2} = \sqrt{\frac{4E_f G_i}{r_f}} \qquad (11)$$

We can see that the debond stress and debond load do not depend on the embedded length, so that this analysis is not satisfactory.

Gao *et al.* [36, 37] included friction in the debonding criterion. The expression of compliance has been calculated on the basis of the shear lag model from fibre displacement at $x = 0$ for a perfect bonding, and the Poisson's contraction of the loaded fibre has been taken into account. Then, the partial debond stress for $r_f \ll R_m$ is given by:

$$\sigma_d^p = \sigma_0 + (\bar{\sigma} - \sigma_0)\{1 - \exp(-\lambda a)\} \qquad (12)$$

with σ_0, the frictionless debond stress given by expression (11), $\bar{\sigma}$ is a function of the clamping residual stress on the fibre q_0, the elastic properties of fibre and matrix and composite geometry, and λ is a function of the friction coefficient μ, the elastic properties of fibre and matrix and composite geometry.

The full debond stress can be obtained by substituting the crack length a by the embedded length L. This time, the debond stress depends on the embedded fibre length.

In a different approach, the strain energy stored in the composite is determined in order to get the energy balance equation.

Piggott [38] proposed an expression of the debond force as a function of the interfacial toughness G_i and the embedded length. Nevertheless, his analysis is not satisfactory because the strain energy in the fibre free length was neglected and because the fracture criterion was not correctly expressed.

Penn and Lee [39] reexpressed the fracture criterion and considered the strain energy stored in the fibre free length to give the energy balance equation:

$$2\pi r_f G_i = \frac{dU_t}{da} + \frac{dU_L}{da} \qquad (13)$$

with U_t, the strain energy stored in the embedded fibre length plus the strain energy stored in the surrounding matrix, and U_L, the strain energy stored in the fibre free length.

Then, the debond force becomes:

$$F_d = 2\pi r_f \sqrt{r_f G_i E_f} \tanh(\alpha L) \qquad (14)$$

with α a constant given by expression (5).

Mai [40] has introduced friction in this analysis leading to an expression of the partial debond stress as a function of the crack length a.

2.3. Friction

Friction occurs when new surfaces are created at the interface. The frictional resistance force is a function of the friction coefficient μ and the clamping residual stress q_0.

In the simplest model, the axial stress required to pull out the fibre is given by [25–28]:

$$\sigma_f = \frac{2\tau_f x}{r_f} = \frac{2\mu q_0 x}{r_f} \qquad (15)$$

When Poisson's contraction of the fiber is considered, the clamping stress decreases and the axial stress is no more linear [41]:

$$\sigma_f = \sigma_{f_0}\{1 - \exp(-\chi x)\} \qquad (16)$$

with σ_{f_0} being a function of the clamping stress on the fibre q_0 and the elastic constant of fibre and matrix, and χ, a function of the friction coefficient μ and elastic properties of fibre and matrix.

Fig. 5 represents the frictional stress distribution in the linear and non linear case. Parameters for the calculation are given in Table I.

It clearly shows that Poisson's contraction must be taken into account for large embedded lengths, even for a small value of the Poisson's ratio. For instance, in the case of a glass fibre with an embedded length of 1 mm, the linear model forecasts fibre failure (the value of the failure strength varies between 1.5 and 3 GPa) whereas the non linear model predicts fibre pull out.

TABLE I Calculation parameters

Modulus (GPa)		ν		Radius (m)				
E_m	E_f	ν_m	ν_f	R_m	r_f	μ	q_0 (MPa)	τ_d (MPa)
3	73	0.4	0.2	$3{\cdot}10^{-3}$	$7{\cdot}10^{-6}$	1.25	10	72.7

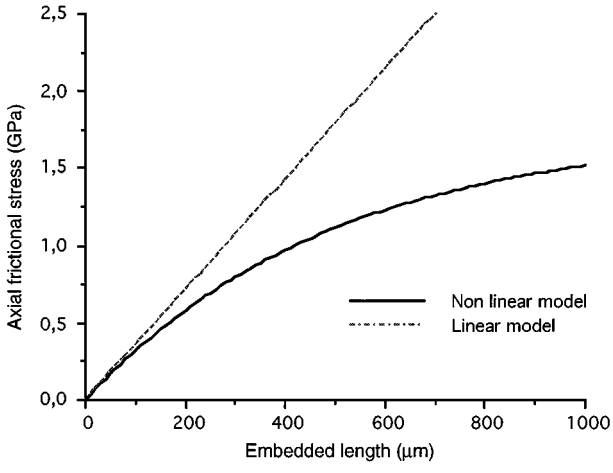

Figure 5 Pull-out stress versus embedded fibre length according to linear and non-linear models.

2.4. Critical comments

The list of above-mentioned models is not exhaustive, but it is representative of the different approaches developped in the last decades. Choosing a model for experimental data analysis is a very difficult task, because the values of interfacial shear strength or interfacial toughness strongly depend on the selected analysis [7].

The mechanical approach based on shear strength criterion and the energic approach based on fracture mechanics criterion have been distinguished. There is no clear justification to use either of these criteria for predicting debonding behavior.

Wells and Beaumont [2] have however shown that the debond stress as a function of the fibre radius is more accurately predicted by the Outwater and Murphy energetic approach.

Other comparisons have been made [37, 42]. For small values of the embedded length, pull-out behavior seems to be better described by an analysis based on a shear strength criterion. Nevertheless, the debond stress is underestimated for large embedded lengths. On the contrary, an approach based on the concept of fracture mechanics better predicts debond behavior for large embedded lengths.

Fig. 6 shows the partial debond stress as a function of debond length L_d for three given embedded lengths $L = 100{,}300{,}500$ μm. Stress computation has been made using a mechanical model developped by Hsueh [31] with the calculation parameters listed in Table I.

For $L = 500$ μm, the partial debond stress first increases with the debonded length. Consequently, when debonding is initiated, further increase of the applied stress is necessary to continue debonding. When the maximum of the partial debond stress is reached, i.e. when $L - L_d = z_{max}$, the interface suddenly fails.

The critical value of the bond length z_{max} is shown to be independent of the embedded length L and it mainly

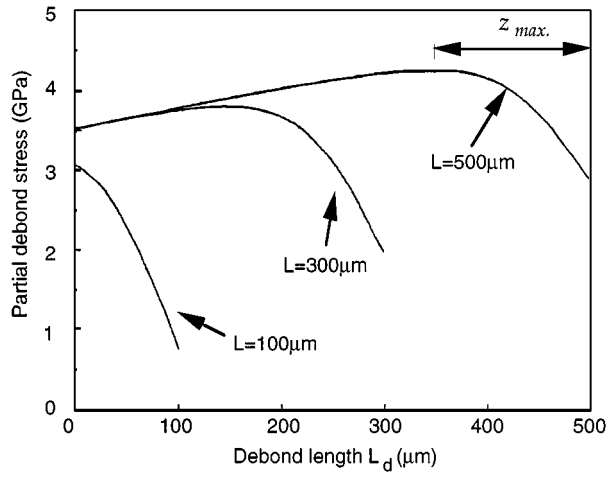

Figure 6 Partial debond stress profiles.

depends on the ratio τ_d/τ_f. A simple expression of z_{max} can be given by assuming a constant frictional shear stress along the debonded length [22]:

$$z_{max} = \frac{1}{\alpha} \cosh^{-1} \sqrt{\frac{\tau_d}{\tau_f}} \quad (17)$$

For embedded lengths below z_{max}, when debonding is initiated, no further increase in applied stress is required to continue the debond process, and thus sudden and complete debonding occurs. Consequently, a mechanical model neglecting friction accurately describes debond behavior for $L \ll z_{max}$.

On the contrary, for large embedded lengths, complete debonding no more occurs suddenly. In this case, the contribution of frictional resistance forces acting over the debonded length must be considered.

Unfortunately, mechanical models which include friction parameters in the expression of the debond stress cannot be satisfactory. Indeed, these models do not consider stress concentration at the crack tip and thus the debond stress is overestimated.

Most energetic approaches assume a stable crack propagation along the interface with a constant value of the interfacial toughness G_i. Consequently, these theories cannot be applied in case of short embedded lengths. On the other hand, when $L \gg z_{max}$, propagation is almost stable and energetic models are satisfactory if friction is taken into account.

In brief, a mechanical theory neglecting friction can be applied to totally unstable debonding, whereas an energetic one can describe stable debonding.

Mai's model [40], which expresses the partial debond stress as a function of the crack length seems to be an interesting way for representing partial debonding. Unfortunately, the expression of debond stress is very complex. Furthermore, evaluation of the interfacial parameters leads to the same values as the ones obtained with a simpler model [36], thus Mai's model turns out to have little practicality.

Consequently, only the two utmost ideal behaviors of stable and unstable debonding can be correctly predicted on basis of theoretical model, but there is no satisfactory model for describing the most current behavior of partial debonding. Therefore, we will choose to compare experimental results to computed data using both a mechanical model neglecting friction and using an energetic analysis taking friction into account. This comparison will give valuable informations about the debond process in our composite systems and so about the relevance of the calculated interfacial parameters.

For the fracture mechanics approach, the Gao *et al.*'s model is chosen. Indeed, in this analysis, the debonding is due to the stable propagation of a crack along the interface and the friction behavior is included.

Fig. 7 shows the distribution of shear stress based on shear strength criterion models for an embedded length $L = 1$ mm and a load $P_0 = 1500$ MPa. The calculation parameters are again those of Table I.

Computed maximum shear stress according to the three theories falls within 1%. This result is similar for a small embedded length. These discrepancies are not significant in consideration of the experimental data scatter. Thus, the simplest analytical expression of the debonding stress is chosen, that corresponds to Lawrence's model.

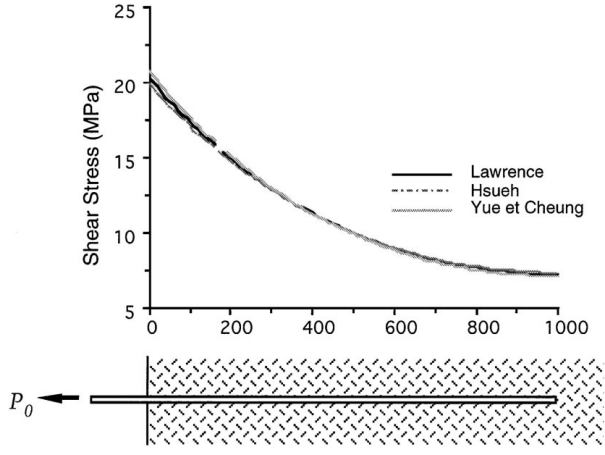

Figure 7 Shear stress distribution according to three mechanical models.

3. Experimental

3.1. Materials

The matrix is an unsaturated polyester resin with Low Profile Additives (LPA) and styrene as curing agent supplied by Cray Valley. The prepolymer (UP) is a 1 : 1 copolymer of maleic anhydride and propylene glycol. Thermoplastic Low Profile Additives (LPA) have been added in the UP resins to compensate for the curing shrinkage. The low profile behavior has been widely discussed in the literature [42–52], and it has been shown that phase separation occurs in styrene-UP-LPA ternary system during curing and that shrinkage compensation is ensured by microvoids formation in the thermoplastic phase. A poly vinyl acetate PVAc and a (methyl methacrylate/methacrylic acid/hydroxylated methacrylate) copolymer PMMA(OH) have been used as Low Profile Additives. They differ by their initial miscibility in UP/styrene mixture, PMMA(OH) being the more miscible additive.

Resin curing was achieved at 90 °C for 30 min, followed by a post-curing treatment for 2 h at 140 °C. Catalytic system varied according to the nature of the Low Profile Additive. It consisted of Perkadox 16 (1.5%) for PVAc additive and Trigonox C (2%) for PMMA(OH) additive.

Sized glass fibres have been supplied by Vetrotex International. The average fibre diameter has been estimated to be 14 μm. Four sizings were available and differing both in film former nature (which was either PVAc or PMMA(OH)) and in their degree of solubility (which expresses the amount of film former bonded to the fibre). The main characteristics of the sizings are summarized in Table II. In that respect systems A and C are referred to as soluble systems whereas B and D are quoted as insoluble.

A more detailed description of materials microstructure will be reported in part II with special emphasis on interface structure in relation to sizing.

TABLE II Sizing characteristics

Specimen	Film former	Solubility[a]
A	PVAc	80%
B	PVAc	20%
C	PMMA(OH)	80%
D	PMMA(OH)	20%

[a]Solubility refers to sizing weight fraction dissolved in toluène.

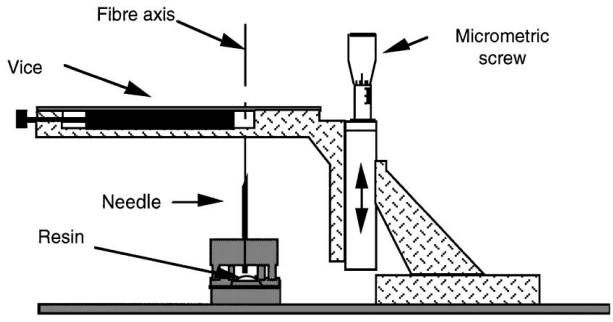

Figure 8 Sample preparation device.

3.2. Pull out testing

The sample preparation has been carried out using the equipment depicted in Fig. 8. The fibre is held above the resin in vertical position by a needle and gripped in a vice. The vertical displacement of the fibre is achieved using a micrometric table. The fibre end is brought into contact with the resin surface, and then the fibre is introduced into the matrix up to the desired embedded length using the micrometric screw. An optical apparatus allows to control this process. Then, matrix curing is achieved following the above-mentioned procedure. If no shrinkage or swelling occurs during curing, sample with controlled embedded length can be obtained using this apparatus.

The pull-out test has been performed on an Instron machine (Fig. 9). The sample is held on the upper crosshead and vertical alignment of the fibre is ensured by a goniometric head and adjusted with the aid of a telescopic sight. The free end of the fiber is embedded in a hot melt sealant laid on an electronic scale. The embedded length in the hot melt sealant is such that debonding and pull-out always occur in the upper part. The scale is used as a load cell, the tensile load on the fiber during the test being monitored as the weight loss on the scale. The crosshead speed has been set at 50 μm/min.

Embedded lengths were measured after the pull-out process. In PVAc systems, the difference between planned and actually measured embedded length did not exceed 20 μm. On the contrary, due to a swelling effect that occurred in systems containing PMMA(OH) as a Low Profile Additive, embedded lengths were systematically measured after pull-out test and data corresponding to fibre failure have not been plotted.

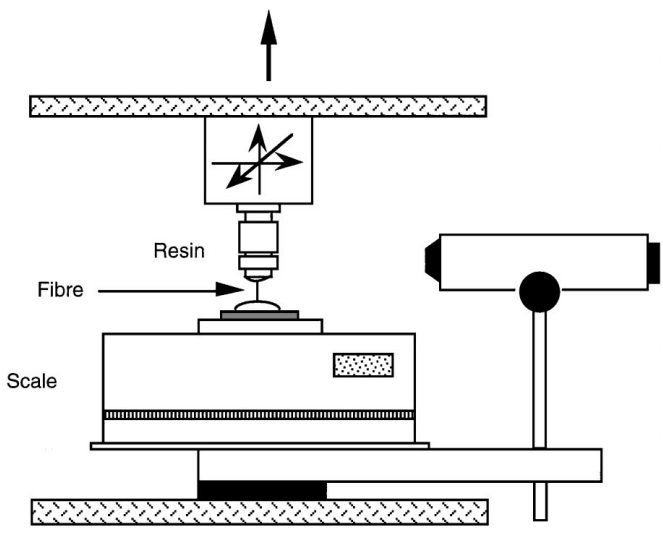

Figure 9 Pull-out testing configuration.

4. Results

4.1. Shape of the pull-out curve

The tensile load on the fibre has been recorded as a function of the displacement of the upper crosshead. Typical experimental pull-out curves are shown in Fig. 10. First, consider the Type 1 pull-out curve depicted in Fig. 10. At the start of the test, the system is elastically loaded, nevertheless the curve does not keep a linear shape and some jerks occasionally occur as the load is increased. These observations indicate that debonding is neither complete nor sudden. When the load maximum is reached, debonding is complete and load abruptly falls. The fibre free length elastic relaxation leads to partial fibre pull out [39]. The second part of the curve corresponds to the fibre pull-out with a pronounced stick-slip phenomenon.

Type 2 pull-out curve also depicted in Fig. 10 was only observed in system D for large embedded lengths. In this case, the curve shows a sequence of rise and

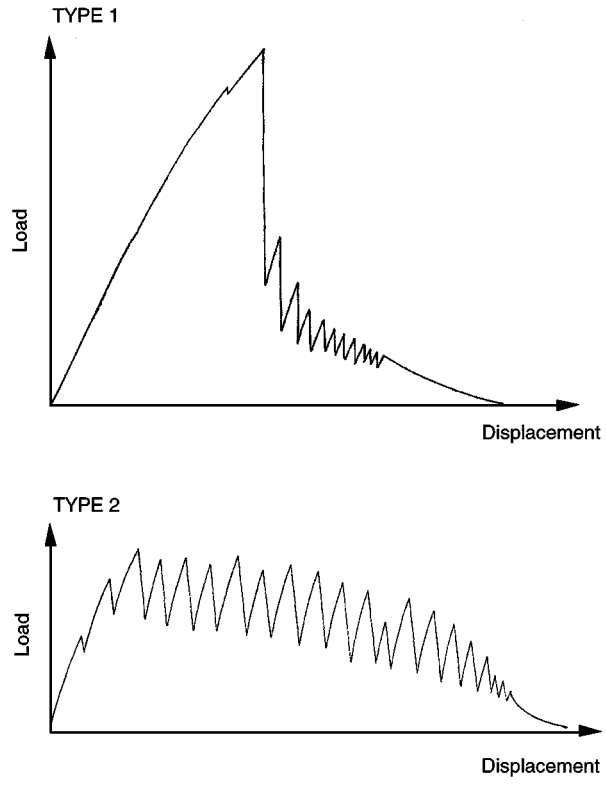

Figure 10 Typical pull-out curves.

fall of the load. Debond and pull-out processes can no more be distinguished so that the debond load cannot be determined. Differentiation between these two kinds of behavior will be made on plots giving the debonding load versus embedded length, and in the case of the latter the reported load will be the recorded maximum load.

4.2. Debond load versus embedded length

4.2.1. PVAc based systems

Plots of debond load versus embedded length are reported on Fig. 11. Generally, the load necessary to debond and pull out the fibre increases with the embedded length, so that fibre failure can occur when the embedded length exceeds a critical value. This critical embedded length is defined by the border-line between fibre pull-out and fibre failure regimes.

It can be seen from Fig. 11a and b that systems A and B cannot be differentiated in term of critical embedded length, which is about 500 μm in both cases. Nevertheless, two types of behaviors can be distinguished. Indeed, in system B, the debond load continuously increases with the embedded length while high values of debond load are already recorded for small values of the embedded length in system A.

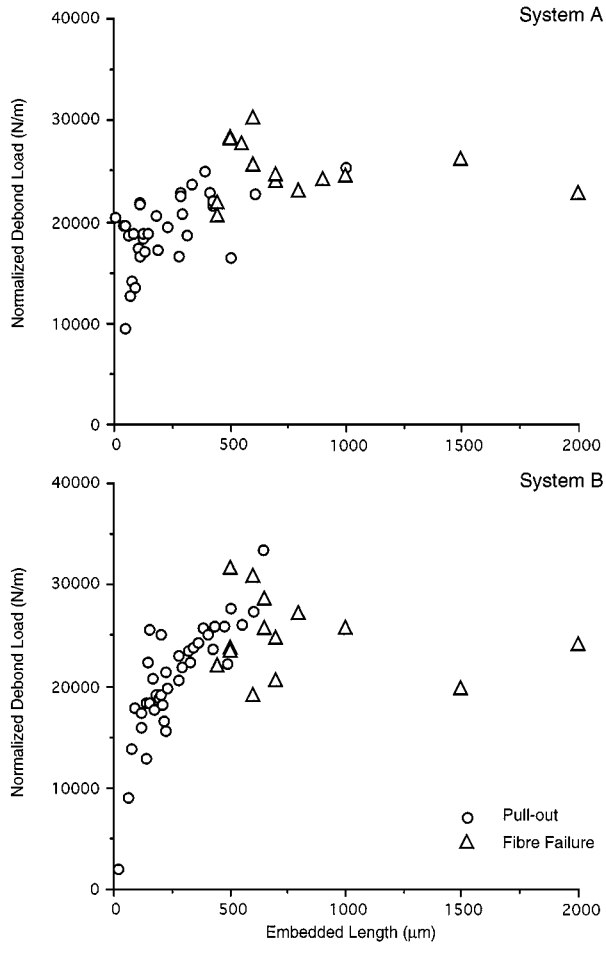

Figure 11 $F_d/2r_f$ versus embedded fibre length for Systems A and B.

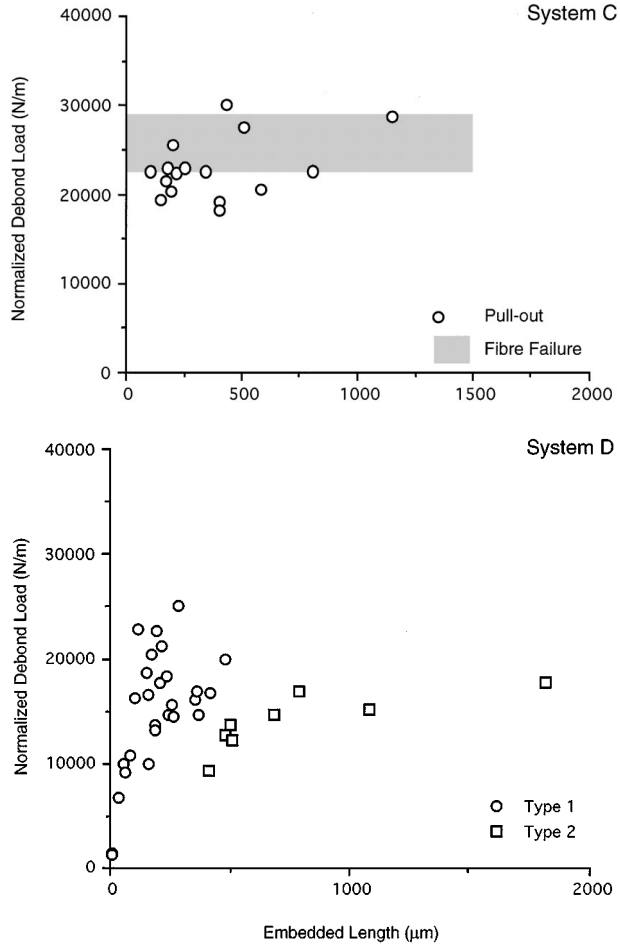

Figure 12 $F_d/2r_f$ versus embedded fibre length for Systems C and D.

4.2.2. PMMA(OH) based systems

Fig. 12 shows the debond load versus embedded length for system C. The load level for which fibre failure occurs is pointed out by a grey strip. The C system shows similar features as system A, i.e. high values of debond load for small embedded lengths.

Results concerning the D system are reported on the same figure. Regarding conventional pull-out data, the debond load increases with embedded length as in B system. For large embedded lengths, pull-out curves show the features of type 2 behaviour in Fig. 10 and the maximum loads are lower than the ones recorded for a value of embedded length equal to 400 μm (Type 1). Note that fibre failure has never been observed. The abrupt change in pull-out behavior can be explained by a microstructure heterogeneity of the matrix at the sample surface. Nevertheless, it does not affect the pull-out behavior of system C. This point will be discussed later.

4.3. Interfacial parameters determination

For the D system, only Type 1 data are considered for the determination of the interfacial parameters.

4.3.1. Lawrence's model

Interfacial parameters are the interfacial shear strength τ_d and the coefficient α. The average shear strength

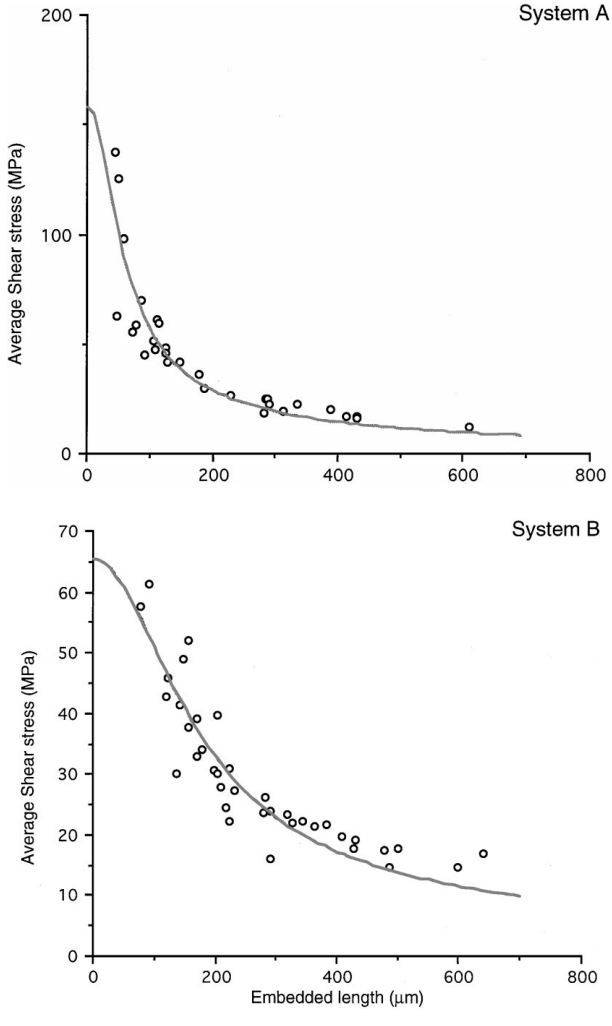

Figure 13 Average shear stress versus embedded length for Systems A and B.

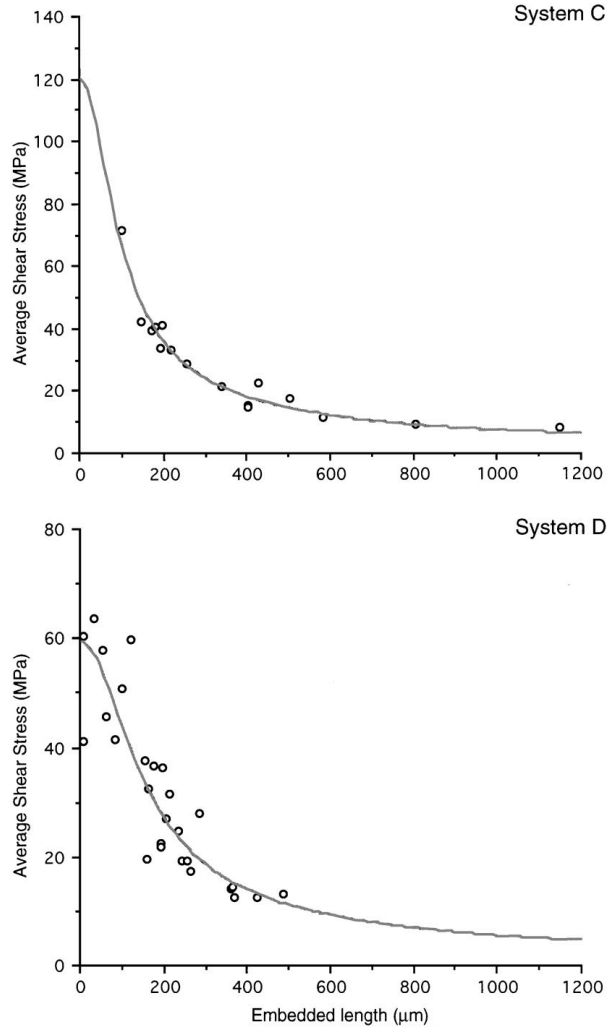

Figure 14 Average shear stress versus embedded length for Systems C and D.

TABLE III Interfacial parameters in Lawrence's analysis

	Ref.	A	B	C	D
τ_d (MPa)	50	160	65	120	60
α	9644	27440	9490	16692	10603

is reported as a function of the embedded fibre length (Figs 13 and 14) and τ_d and α are fitted to experimental results using Equation 4:

$$\tau_a = \frac{F_d}{2\pi r_f L} = \tau_d \frac{\tanh(\alpha L)}{\alpha L} \quad (4)$$

Results are summarized in Table III and compared to reference values. The matrix shear strength is estimated to 50 MPa and α is computed using Equation 5 and data from Table I.

Regarding insoluble systems B and D, a good agreement between theoretical and experimental values is obtained. On the contrary, the debond shear strength in systems A and C widely exceeds the matrix shear strength. Consequently the values of these interfacial parameters are unrealistic and Lawrence's model is not suitable to describe the behavior of soluble systems A and C. Therefore, the comparison of experimental results to Lawrence's model shows a differentiation in terms of the degree of sizing solubility.

4.3.2. Gao et al.'s model

Interfacial parameters are the interfacial toughness G_i, the clamping stress q_0 and the friction coefficient μ. The determination of Gao *et al.* interfacial parameters is detailed in Appendix. q_0 and μ are first determined using the second part of the pull-out curve (Fig. 10 type 1) and the friction stress is reported as a function of the embedded fibre length (Figs 15 and 16). Then, the calculated values of q_0 and μ are reintroduced to determine the interfacial toughness G_i from plots of the debond stress versus the embedded length (Figs 17 and 18). Results are summarized in Table IV.

The friction behavior is notably affected by the nature of the sizing in PVAc systems, while the values

TABLE IV Interfacial parameters in Gao *et al.*'s analysis

	A	B	C	D
μ	5	2	2	1.5
q_0 (MPa)	10	15	10	10
G_i (J/m^2)	110	65	180	30

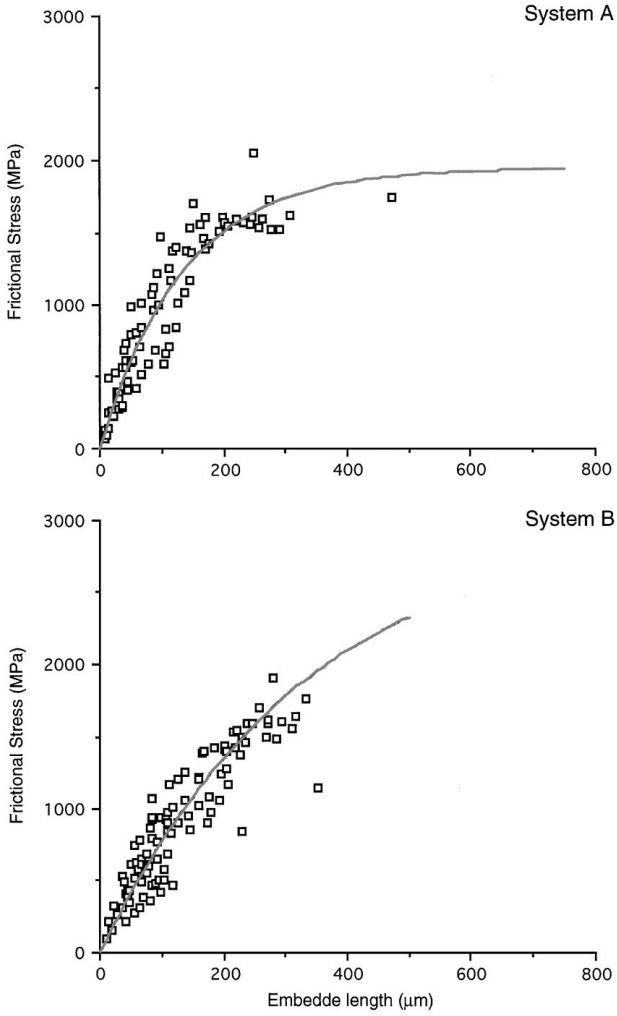

Figure 15 Frictional stress versus embedded length for Systems A and B.

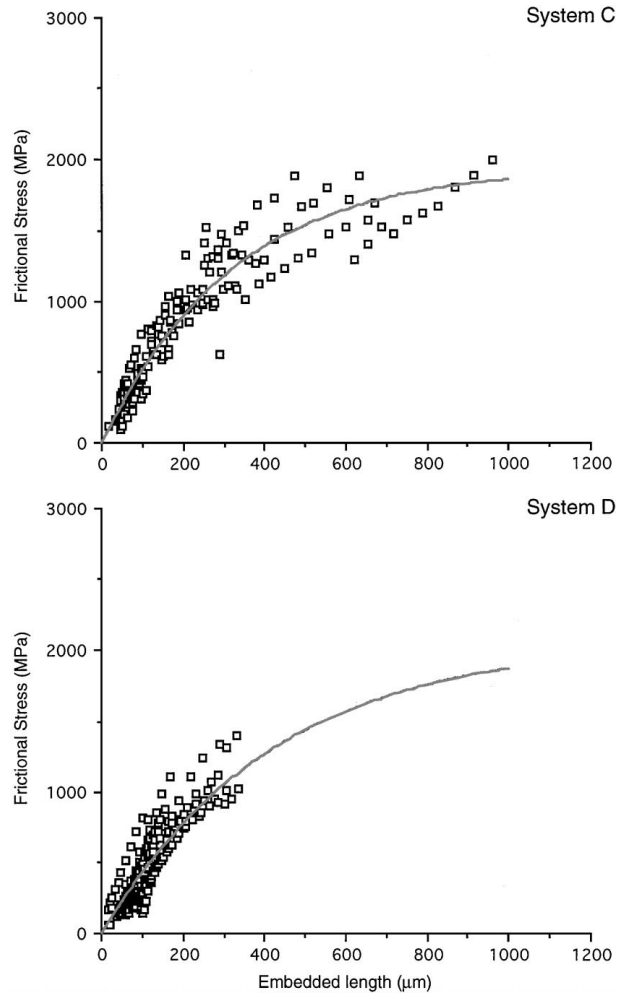

Figure 16 Frictional stress versus embedded length for Systems C and D.

are almost the same in PMMA(OH). Regarding the interfacial toughness, once again the degree of sizing solubility seems to be a determining parameter on the debonding process. For soluble sizings, this model provides a good agreement between experimental results and theoretical curve, while Lawrence's model was not satisfactory for these systems. On the contrary, the small embedded lengths are not correctly taken into account for insoluble sizings (Fig. 18).

5. Discussion

Results suggest that the interfacial response is mainly affected by the sizing nature, especially its degree of solubility.

In soluble systems, it has been shown that Lawrence's model leads to inconsistent values of interfacial parameters, so it cannot be applied to these systems. On the other hand, Gao *et al.*'s model provides a good fit between theory and experimental data. The latter is not true for insoluble systems where the model based on fracture mechanics criterion always overestimates the debond stress for short embedded length while Lawrence's mechanical model describes fairly well the debonding process over the whole range of embedded fibre lengths.

5.1. Debonding process

In the first part of this work, it has been pointed out that a model based on a shear strength criterion which neglects friction effects is suitable for describing a totally unstable and complete debonding process, while a model based on a fracture mechanics criterion which takes friction into account is satisfactory in the case of a totally stable debonding. This statement leads to fundamental conclusions about the debonding process in our composite systems: the debonding is rather unstable in insoluble systems and rather stable in soluble systems.

Nevertheless, stability of the debonding process does not only depend on the nature of the interface. The relative degree of agreement obtained between theories and experiments also depends on embedded fibre lengths. Gao *et al.*'s model predicts the magnitude of the debond stress σ_d fairly well for long embedded lengths L but overestimates σ_d at small L. In contrast, Lawrence's model satisfactory forecasts σ_d for short L and tends to underestimate slightly σ_d as L is increased.

The border line between complete and partial debonding is given by z_{max}. This critical length can be estimated using Equation 17. In soluble systems A and C, the values of α and τ_d are not available, thus z_{max} is computed using reference data from Table III. Results are given in Table V.

TABLE V Estimate of z_{max}

	A	B	C	D
z_{max} (μm)	~0	100	100	130

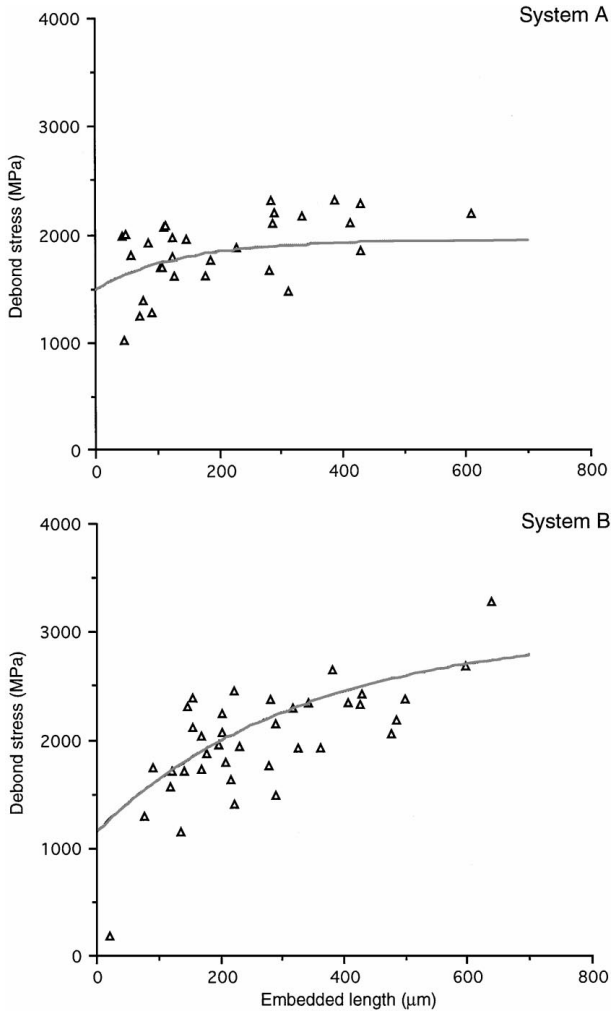

Figure 17 Debond stress versus embedded length for Systems A and B.

For PVAc based systems, the values of z_{max} are strongly different, which supports the above conclusions about the stability of debonding in relation to sizing solubility. This difference is not as pronounced in PMMA(OH) based systems.

Since both theories are not suitable for predicting the debond stress over the whole range of embedded fibre lengths, a second evaluation of interfacial parameters is made.

Application of Gao *et al.*'s model is reconsidered only for large embedded lengths. Results are given in Table VI.

Once again the difference between the two evaluations is more pronounced in PVAc based systems than in

TABLE VI Values of G_i (J/m^2)

	A	B	C	D
First evaluation	110	65	180	30
Second evaluation	140	20	180	40

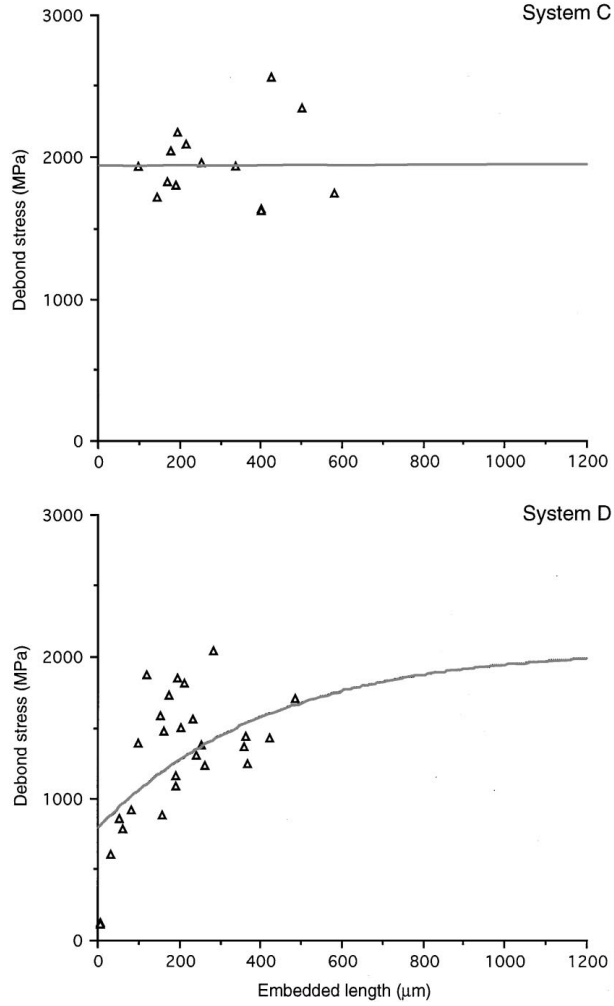

Figure 18 Debond stress versus embedded length for Systems C and D.

PMMA(OH) based systems. Since frictional resistance forces are very high in PVAc based systems, interfacial toughness is overestimated when the whole range of embedded lengths is taken into account. In contrast, in PMMA(OH) based systems, frictional parameters are lower, so a second fit does not lead to great variations in the final result.

Regarding Lawrence's model, any significant change in the derived values of τ_d and α is obtained when

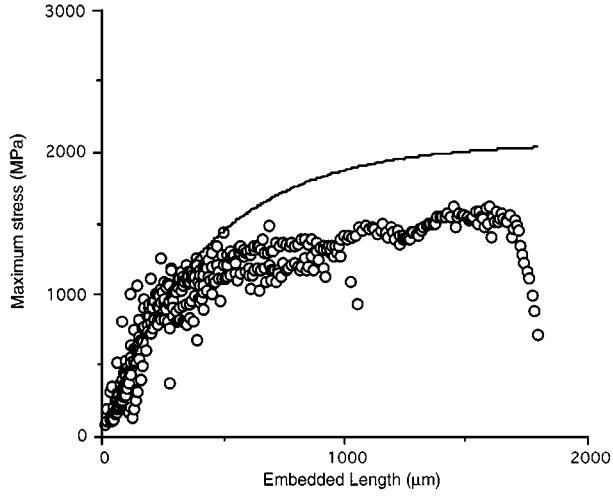

Figure 19 Maximum stress versus embedded length for System D.

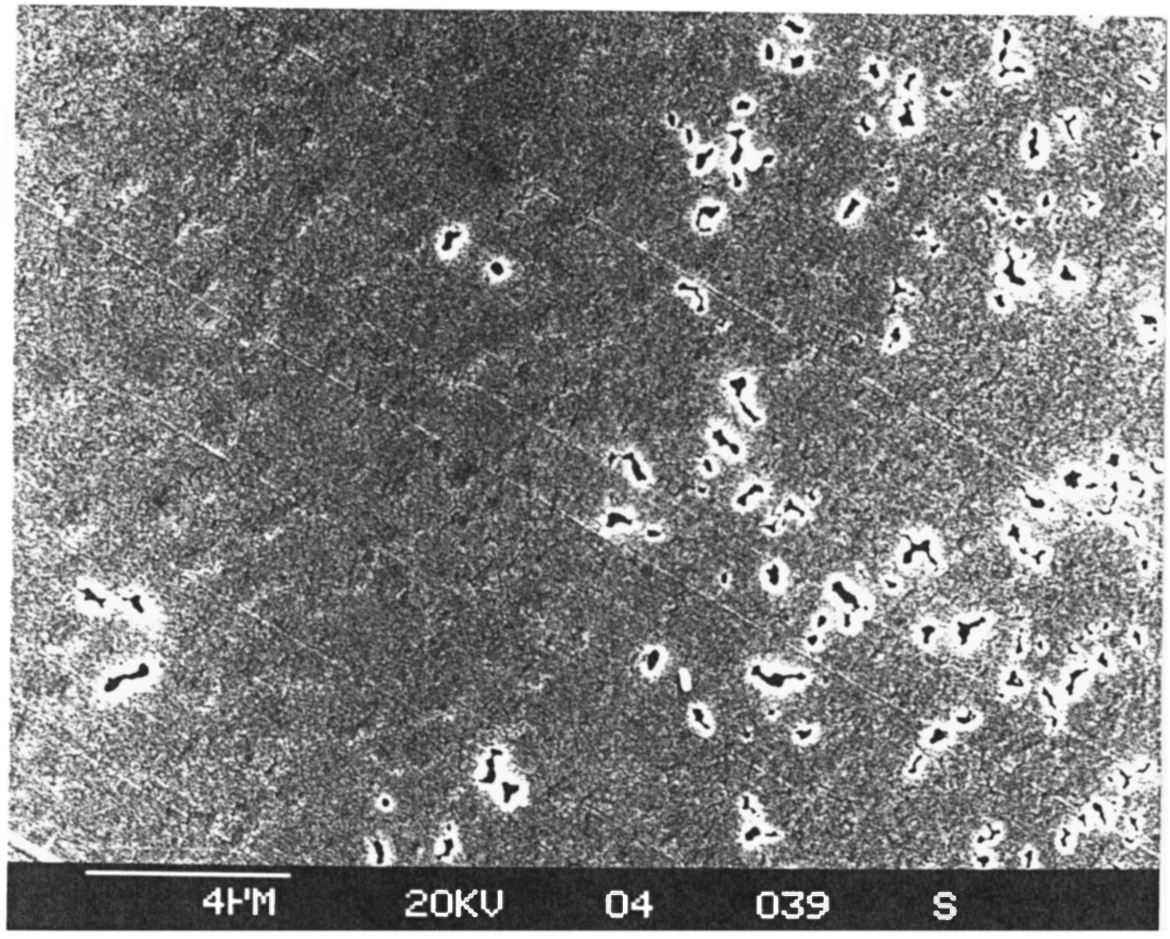

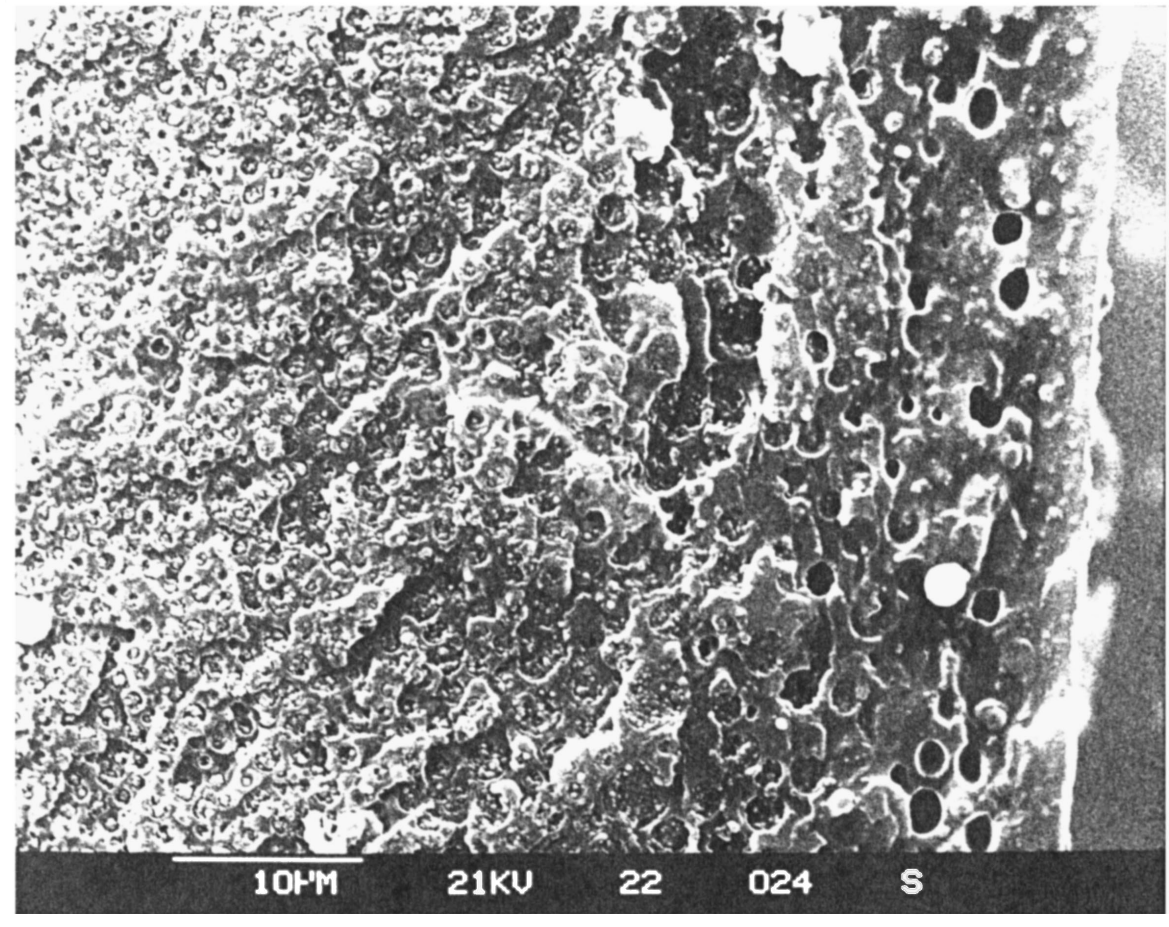

Figure 20 Sample surface morphology: (a) microtomed specimen, (b) fracture surface.

only small embedded fibre lengths are taken into account for insoluble systems B and D. Thus, Lawrence's model appears to be very satisfactory for describing the debonding process in these systems, even if the fitting curve diverges from experimental data as L increases. For soluble systems A and C, a second fit is not possible since data for small embedded fibre lengths are not available.

The second evaluation of interfacial parameters reinforces our preliminary conclusions. Either Lawrence's model or Gao *et al.*'s model are unable to provide a satisfactory answer over the whole range of embedded fibre lengths, but the confrontation of these models to experimental results end up with a rather clear picture of the debonding process. Indeed, it has been shown that the trend of debonding process is unstable for insoluble systems B and D and stable for soluble systems A and C.

The comparison between experimental data and those simple models either based on a mechanical criterion or a fracture mechanics criterion thus proves to be a very attractive way for the interpretation of pull-out test and consequently the use of more complex theories is not quite justified.

5.2. Matrix microstructural heterogeneity in PMMA(OH) based systems

Results concerning system D have shown two kinds of behavior depending on the embedded fibre lengths. For small embedded length (below 500 μm), Type 1 conventional pull-out curves are observed. For larger embedded lengths, the pull-out curves show a sequence of rise and fall of the load. The maxima of Type 2 pull-out curves are reported as a function of the embedded length in Fig. 19 and compared with the frictional stress (computed using the following values $\mu = 1.5$ and $q_0 = 10$ MPa). Once again a change in pull-out behavior is revealed at $L = 500$ μm. The recorded stress level is always below the frictional stress when the embedded length exceeds a critical value, thus all interfacial parameters are modified from this critical depth.

It is thus worth looking for the existence of a microstructural heterogeneity in order to explain this change in pull-out behavior as the embedded length is increased. Consequently, the matrix morphology at the sample surface is investigated by scanning electron microscopy. A specimen is microtomed and gold-coated in order to reveal the presence of cavities. Another one is broken into several pieces and then etched in dichloromethane to dissolve the soluble material on the fracture surfaces in order to reveal the macrogels.

The scanning electron micrograph of Fig. 20a clearly shows the typical morphological features of a two phase UP resin/LPA system. Indeed, it reveals the presence of LPA composites particles, each containing numerous UP subinclusions in a polyester matrix. It is also seen that particle sizes decrease as the depth from the sample surface increases. No microvoids have been revealed at the sample surface, nevertheless cavities appear up to a certain depth. The discontinuity is clearly shown on Fig. 20b. These observations indicate the presence of a miscibility gradient at the sample surface. This change in miscibility may be due to the styrene evaporation during pull-out sample preparation and matrix curing.

The matrix heterogeneity is clearly revealed in PMMA(OH) based systems. Two questions arise from this observation. The first one is to determine how this matrix heterogeneity interacts with the pull-out behavior of system D and the second is to understand why it does not affect the pull-out behavior of system C.

For system D, the above results obtained from Type 1 data show that the debonding is almost unstable. Crack initiation requires a high stress level but its propagation is relatively easy. For large embedded fibre lengths ($L > 500$ μm), the presence of cavities near the interfacial region can promote crack initiation and interfacial debonding can occur at a lower stress level as it has been observed.

Regarding system C, it has been established that debonding is almost stable. Consequently, even if crack initiation is promoted for large embedded fibre lengths, its propagation along the interface requires a high stress level. Moreover, the critical embedded fibre length (from which fibre failure occurs) is about 500 μm, which correspond to the border-line between the two types of behavior in system D. For these reasons, no discontinuity in the pull-out behavior is observed for this system.

The micromechanical implication of matrix heterogeneity in PMMA(OH) based systems leads us to reconsider the PVAc based systems. The same morphological study has been carried out on the latter. No change in system miscibility has been observed at the sample surface and no cavitation has been revealed down to a depth of about 1 mm (which is above the critical embedded fibre length for these systems).

A closer look at the correlation between mechanical behavior and the local interface microstructure will be given in the second part of this paper.

6. Conclusion

Based on a critical review, two distinct approaches for the interpretation of pull-out test data have been selected. The first one based on a mechanical criterion is satisfactory for describing unstable debonding while the second predicts well a stable crack propagation along the interface.

Four composite systems have been studied. Results have shown that sizing solubility is a major parameter which determines the debonding behavior.

This micromechanical study provides interesting results regarding the debonding process. In soluble systems A and C, the debonding is almost stable while it is almost unstable in insoluble systems B and D.

As a secondary effect, a change in pull-out behavior has been observed for embedded fibre lengths above 500 μm in system D. This discontinuity has been attributed to the matrix microstructural heterogeneity near the sample surface. No change in behavior has been observed for system C due to the debonding stability in this system.

Appendix

Gao *et al.* expressed the partial debond stress as:

$$\sigma_d^p = \sigma_0 + (\bar{\sigma} - \sigma_0)\{1 - \exp(-\lambda L_d)\} \quad \text{(A1)}$$

with

$$\sigma_0 = \sqrt{\frac{4E_f G_i}{r_f(1 - 2k\nu_f)}} \quad \text{(A2)}$$

$$\lambda = \frac{2\mu k}{r_f} \quad \text{(A3)}$$

$$\bar{\sigma} = -\frac{q_0}{k}\left(1 + \frac{\gamma}{\varphi}\frac{\nu_m}{\nu_f}\right) \quad \text{(A4)}$$

$$\varphi = \frac{E_m}{E_f} \quad \text{(A5)}$$

$$\gamma = \frac{r_f^2}{R_m^2 - r_f^2} \quad \text{(A6)}$$

$$k = \frac{\varphi\nu_f + \gamma\nu_m}{\varphi(1 - \nu_f) + 1 + \nu_m + 2\gamma} \quad \text{(A7)}$$

Debonding is complete when $L_d = L$ and then the total debond stress is given by:

$$\sigma_d = \sigma_0 + (\bar{\sigma} - \sigma_0)\{1 - \exp(-\lambda L)\} \quad \text{(A8)}$$

When debonding is complete, only frictional resistance forces act over the debonded length. The friction stress is obtained by replacing σ_0 by 0 in Equation A8.

$$\sigma_f = \bar{\sigma}\{1 - \exp(-\lambda L)\} \quad \text{(A9)}$$

The first part of the pull-out curve (Fig. 21) corresponds to the debond process. When the maximum load is reached, debonding is complete. The maximum load F_d leads to the total debond stress.

The abrupt fall in load after debonding leads to a partial fibre pull-out. Penn and Lee [39] have shown that the partial pull-out fibre length is equal to the displacement u_1 of the upper crosshead.

Consequently, the recorded load F_{f_1} is not the load required to pull-out a fibre with an embedded length equal to L but equal to $(L - u_1)$, as F_{f_2} is the load required to pull out a fibre with an embedded length $(L - u_2)$, etc. Then, the frictional stress is reported as a function of $(L - u_i)$. The determination of both the friction coefficient and the clamping stress is based on these data using the following equation:

$$\sigma_{f_i} = \bar{\sigma}\{1 - \exp[-\lambda(L - u_i)]\} \quad \text{(A10)}$$

The calculated values of frictional parameters are reintroduced to determine the interfacial toughness from the plot of debond stress versus embedded length using Equation A8 and elastic constants of Table I.

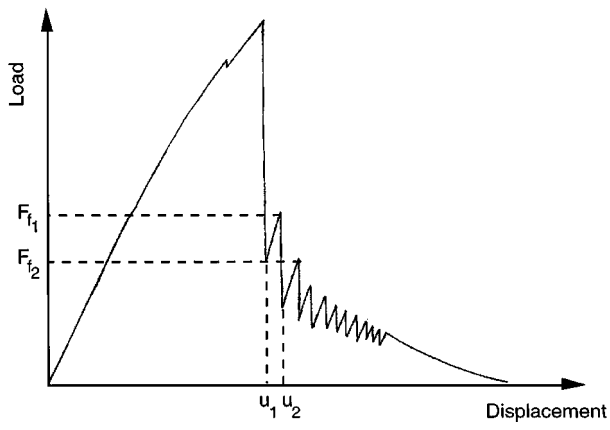

Figure 21 Gao *et al.*'s parameters determination.

Acknowledgements

This work has been performed with the support of Cray Valley (C.V.) and Vetrotex International (V.I.). Fruitful discussions with J. C. Jannel, J. P. Lecointe, C. Wrotecki (C.V.) and D. Muller (V.I.) are gratefully acknowledged.

References

1. J. N. KIRK, M. MURO and P. W. R. BEAUMONT, *J. Mater. Sci.* **13** (1978) 2197.
2. J. K. WELLS and P. W. R. BEAUMONT, *ibid.* **20** (1985) 1275.
3. J. O. OUTWATER and M. C. MURPHY, in Proceedings of 24th ANTECH, New York, 1969 (SPI, New York, 1969) Paper 11C.
4. T. U MARSTON, A. G. ATKINS and D. K. FELBECK, *J. Mater. Sci.* **9** (1974) 447.
5. C. Y. YUE and W. L. CHEUNG, *ibid.* **27** (1992) 3843.
6. D. HULL, "An Introduction to Composites Materials" (Cambridge University Press, 1981).
7. M. J. PITKETHLY, J. P. FAVRE, U. GAUR, J. JAKUBOWSKI, S. F. MUDRICH, D. L. CALDWELL, L. T. DRAZL, M. NARDIN, H. D. WAGNER, L. DI LANDRO, A. HAMPE, J. P. ARMISTEAD, M. DESEAGER and I. VERPOEST, *Composites Sci. Technol.* **48** (1993) 205.
8. P. J. HERRERA-FRANCO and L. T. DRZAL, *Composites* **23** (1992) 2.
9. F. HOECKER and J. KARGER-KOCSIS, *ibid.* **25** (1994) 729.
10. L. T. DRZAL and M. MADHUKAR, *J. Mater. Sci.* **28** (1993) 569.
11. J. ANDERSONS and V. TAMUZS, *Composites Sci. Technol.* **48** (1993) 57.
12. J. K. KIM, L. ZHOU and Y. W. MAI, *J. Mater. Sci.* **28** (1993) 6233.
13. M. NARKIS and E. J. H. CHEN, *Polym. Compos.* **9** (1988) 245.
14. M. C. ANDREWS, R. J. DAY, A. K. PATRIKIS and R. J. YOUNG, *Composites* **25** (1994) 482.
15. V. RAO, P. HERRERA-FRANCO, A. D. OZZELLO and L. T. DRZAL, *J. Adhesion* **34** (1991) 65.
16. J. P. FAVRE and D. JACQUES, *J. Mater. Sci.* **25** (1990) 1373.
17. M. KUNTZ, K. H. SCHLAPSCHI, B. MEIER and G. GRATHWOHL, *Composites* **25** (1994) 477.
18. J. P. FAVRE, A. VASSEL and C. LACLAU, *ibid.* **25** (1994) 482.
19. D. KELLY and W. R. TYSON, *J. Mech. Phys. Solids* **13** (1965) 329.
20. L. B. GRESZCZUK, *Interface in Composites*, ASTM STP **452** (1969) 42.
21. R. J. GRAY, *J. Mater. Sci.* **19** (1984) 861.
22. P. LAWRENCE, *ibid.* **7** (1972) 1.
23. H. L. COX, *Brit. J. Appl. Phys.* **3** (1952) 72.
24. A. TAKAKU and R. G. C. ARRIDGE, *J. Phys. D: Appl. Phys.* **6** (1973) 2038.
25. C. Y. YUE and W. L. CHEUNG, *J. Mater. Sci.* **27** (1992) 3173.
26. W. L. CHEUNG, PhD thesis, University of Hong Kong, 1990.

27. A. N. GENT and G. L. LIU, *J. Mater. Sci.* **26** (1991) 2467.
28. A. N. GENT and C. L. SHAMBARGER, *ibid.* **29** (1994) 2107.
29. C. H. HSUEH, *J. Mater. Sci. Lett.* **7** (1988) 497.
30. G. DÉSARMOT, J. P. FAVRE, *Composites Sci. Technol.* **42** (1991) 151.
31. C. H. HSUEH, *Mater. Sci. Eng.* **A123** (1990) 1.
32. C. H. HSUEH, *ibid.* **A123** (1990) 67.
33. C. H. HSUEH, *J. Mater. Sci.* **29** (1994) 1801.
34. C. H. HSUEH, *ibid.* **29** (1994) 5135.
35. H. STANG, S. P. SHAH, *ibid.* **21** (1986) 953.
36. Y. C. GAO, Y. W. MAI and B. COTTERELL, *J. Appl. Math. Phys.* (ZAMP) **39** (1988) 550.
37. J. K. KIM, C. BAILLIE and Y. W. MAI, *J. Mater. Sci.* **27** (1991) 3143.
38. M. R. PIGGOTT, *Composites Sci. Technol.* **30** (1987) 295.
39. L. S. PENN and S. M. LEE, *J. Comp. Technol. Res.* JCTRER **11** (1989) 23.
40. L. M. ZHOU, J. K. KIM and Y. M. MAI, *J. Mater. Sci.* **27** (1992) 3155.
41. D. J. PINCHIN and D. TABOR, *J. Mater. Sci.* **13** (1978) 1261.
42. V. A. PATTISSON, R. R. HINDERSINN and W. T. SCHWARTZ, *J. Appl. Polym. Sci.* **18** (1974) 2763.
43. V. A. PATTISSON, R. R. HINDERSINN and W. T. SCHWARTZ, *ibid.* **19** (1975) 2763.
44. C. B. BUCKNALL, P. DAVIES and I. K. PARTRIDGE, *Polymer* **26** (1985) 109.
45. T. MITANI, H. SCHIRAISHI, K. HONDA and G. E. OWEN, 44th Annual Conf., Composites Institute, SPI (1989) 12-F.
46. L. SUSPÈNE, D. FOURQUIER and Y. S. YANG, 45th Annual Conf., Composites Institute (SPI, 1990) p. 11-F.
47. C. B. BUCKNALL, I. K. PARTRIDGE and M. J. PHILLIPS, *Polymer* **32** (1991) 636.
48. Idem, *ibid.* **32** (1991) 786.
49. L. SUSPÈNE and D. FOURQUIER, *ibid.* **32** (1991) 1593.
50. M. KINKELAAR, B. WANG and L. J. LEE, *ibid.* **35** (1994) 3011.
51. V. GUILLON, Thèse de Doctorat Université des Sciences et Technologies de Lille, 1994.
52. L. SUSPÈNE and Y. S. YANG, 45th Annual Conf., Composites Institute (SPI, 1990) p. 7-C.

Received 29 July
and accepted 29 September 1998